



Direct Numerical Simulation Modeling of Bilayer Cathode Catalyst Layers in Polymer Electrolyte Fuel Cells

Partha P. Mukherjee* and Chao-Yang Wang**,:z

Electrochemical Engine Center and Department of Mechanical and Nuclear Engineering,
The Pennsylvania State University, University Park, Pennsylvania 16802, USA

A pore-scale description of species and charge transport through a bilayer cathode catalyst layer (CL) of a polymer electrolyte fuel cell using a direct numerical simulation (DNS) model is presented. Two realizations of the bilayer catalyst layer structure are generated using a stochastic reconstruction technique with varied electrolyte and void phase volume fractions. The DNS calculations predict that a higher electrolyte phase volume fraction near the membrane-CL interface provides an extended active reaction zone and exhibits enhanced performance. A higher void phase fraction near the gas diffusion layer aids in better oxygen transport. The effects of cell operating conditions in terms of low inlet relative humidity and elevated cell operating temperature on the bilayer CL performance are also investigated. Low humidity and elevated temperature operations exhibit overall poorer performance compared to the high humidity and the low-temperature operations, respectively.

© 2007 The Electrochemical Society. [DOI: 10.1149/1.2776221] All rights reserved.

Manuscript submitted March 16, 2007; revised manuscript received July 2, 2007. Available electronically September 6, 2007.

Despite tremendous progress in recent years, the major performance limitation in polymer electrolyte fuel cells (PEFCs) is still primarily owing to the sluggish kinetics of the oxygen reduction reaction (ORR) as well as several transport losses involving species and charge transfer in the cathode catalyst layer (CL). The state-of-the-art cathode CL is a three-phase composite, consisting of: (i) platinum-supported carbon particles, i.e., the electronic phase for electron transfer; (ii) the electrolyte phase, typically Nafion, for proton transport; and (iii) the void/pore phase for species transport. Gottesfeld and Zawodzinski¹ and, more recently, Eikerling et al.² provided good overviews of the catalyst layer structure and functions. Several competing transport mechanisms prevalent within the cathode CL require an optimal balance among the constituent phases in order to achieve the best cell performances. For example, an increase in Nafion content improves proton conductivity while reducing the available pore space for oxidant transport, resulting in significant decline in the gas phase diffusivity. An increase in Pt loading causes enhanced electrochemical reaction rate, which is however limited by increase in cost. Another important factor affecting the PEFC performance is the involvement of water transport in the cathode CL, via water production due to the ORR as well as migration from the anode side by electro-osmotic drag. Good proton conductivity requires hydration of the electrolyte phase, which is again strongly dependent on the cell operating conditions in terms of the inlet relative humidity as well as the cell operating temperature. It is therefore evident that achieving an enhanced cell performance warrants detailed understanding of the dependence of the cathode CL performance on its composition as well as on the cell operating conditions.

Several experimental and numerical studies have been reported in the literature on the CL composition in order to enhance its performance.³⁻¹⁶ The emphasis of these studies was mainly to investigate the influence of Nafion content, Pt loading, and CL thickness on its performance and suggest the corresponding optimum values for the best performance of single-layer CLs with uniform distribution of Nafion content and Pt loading. Recently, improved performance has been identified with functionally graded cathode CLs in terms of graded distributions of Nafion content and Pt loading.¹⁷⁻²⁰ However, the computational models deployed thus far in the literature are mainly based on the macroscopic theory of volume averaging and can be further distinguished as the homogeneous model and agglomerate model. Recently, Wang²¹ provided a comprehensive overview of the various catalyst layer models. Furthermore, no

model has been attempted to study the electrochemically coupled transport phenomena in a bilayer cathode CL based on pore-level description of species and charge transport.

In the current work, a pore-scale model is presented, based on our direct numerical simulation (DNS) approach²²⁻²⁵ for oxygen, water, and proton transport through a three-dimensional (3-D), bilayer catalyst layer microstructure. The statistically rigorous, 3-D description of the CL microstructure is realized using the stochastic reconstruction technique developed in our earlier work in Ref. 24. The pore-level description of the underlying transport phenomena through different realizations of the bilayer cathode CL is presented. Finally, the salient predictions from the present DNS model are furnished elucidating the trifold influence of the CL structure, composition, and cell operating conditions on the performance.

Model Description

The DNS model is based on the idea that the charge and species transport equations are solved directly on a realization of the CL microstructure. The pore-scale description of transport through the CL porous structure, therefore, does not involve any constitutive relations for the effective transport properties based on the effective medium approximation via Bruggeman-type correlations, otherwise employed in the macrohomogeneous CL models. The DNS model, therefore, comprises two steps: (i) the CL structure generation and (ii) the solution of the electrochemically coupled transport equations directly on the generated structure.

Catalyst layer structure generation.—In the present work, the three-phase CL composite is delineated as a two-phase, porous structure consisting of a mixed electronic/electrolyte phase, i.e., the solid phase and the void phase. This assumption can be justified from the electrochemical perspective of assumed uniformity in the electronic phase potential because the CL is very thin and the electronic phase conductivity is very high, thereby the electron transfer can be neglected. The electronic and electrolyte phases could therefore be lumped together into a mixed solid phase with the ionic phase conductivity duly adjusted with respect to the electronic phase volume fraction. Henceforth, the mixed electronic/electrolyte phase will be referred to as simply the electrolyte phase in the rest of this paper.

In the present study, the CL microstructure is reconstructed using a stochastic generation method. The low cost and high speed of data generation in addition to the apparent resolution constraint of the current experimental imaging techniques make the digital structure generation for the thin CL ($\sim 10 \mu\text{m}$) as the obvious choice.

The stochastic simulation technique relies on the idea that an arbitrary porous medium can be described by a binary phase func-

* Electrochemical Society Student Member.

** Electrochemical Society Active Member.

z E-mail: cwx31@psu.edu

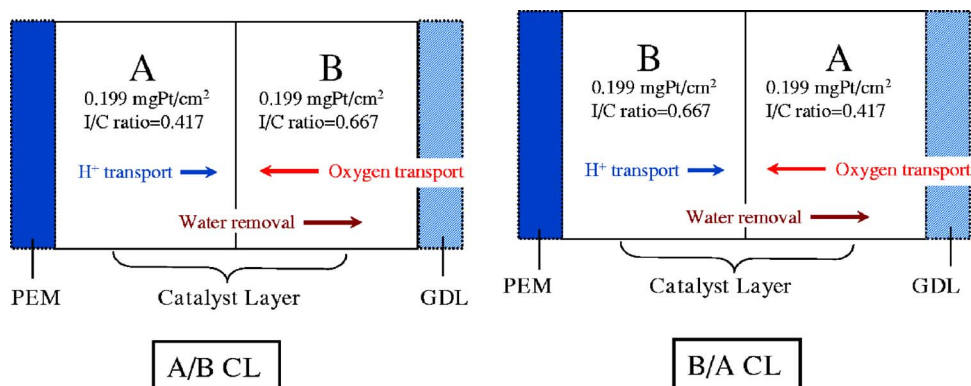


Figure 1. (Color online) Schematic diagram of the A/B and B/A CLs.

tion $Z(\vec{r})$, at each point \vec{r} within the 3-D space, which takes a value of 0 within the void phase and a value of 1 in the solid phase. The discrete, binary phase function is given by²⁶

$$Z(\vec{r}) = \begin{cases} 0 & \text{if } \vec{r} \text{ in the void phase} \\ 1 & \text{if } \vec{r} \text{ in the solid phase} \end{cases} \quad [1]$$

For a statistically homogeneous porous medium, the phase function can be adequately bound by the first two statistical moments, namely, the porosity ε and the two-point autocorrelation function $R_Z(\vec{u})$. The first moment, i.e., porosity, denotes the probability that a point is in the pore space and is defined as the statistical average of the phase function²⁶

$$\varepsilon = \overline{Z(\vec{r})} \quad [2]$$

The two-point autocorrelation function refers to the probability that two voxels at a distance \vec{r} are both in the pore space and can be defined as²⁶

$$R_Z(\vec{u}) = \frac{\overline{[Z(\vec{r}) - \varepsilon][Z(\vec{r} + \vec{u}) - \varepsilon]}}{\varepsilon - \varepsilon^2} \quad [3]$$

where the overbar denotes statistical average and \vec{u} is the lag vector. For a *statistically homogeneous and isotropic porous medium*, ε is constant and $R_Z(\vec{u})$ is only a function of the norm of the lag vector, \vec{u} , i.e., directionally independent of the location vector \vec{r} . The autocorrelation function is evaluated using the image processing technique originally proposed by Berryman²⁷ from a two-dimensional (2-D) transmission electron microscope (TEM) image of an actual CL sample fabricated in-house and characterized using the university TEM facility. The resolution of the 2-D images is set at 512×512 pixels, which was reported to be sufficient for optimum phase resolution.²⁷ The porosity is obtained from the mass loading data of the constituent components available from the CL fabrication process and will be described later. With these two inputs, the reconstruction model generates a 3-D, binary (pore/solid) realization of the CL structure by filtering an initial Gaussian distribution of the phase function with the autocorrelation function and, finally, thresholding the distribution with respect to the porosity. The details of the stochastic reconstruction model can be found in Ref. 24.

The pore/solid phase is further distinguished as “transport” and “dead” phase. The basic idea is that a pore phase unit cell surrounded by solid phase-only cells does not take part in species transport and, hence, in the electrochemical reaction and can therefore be treated as a dead pore and similarly for the electrolyte phase. The interface between the transport pore and the transport electrolyte phases is referred to as the electrochemically active area (ECA) and the ratio of ECA and the nominal CL area provides “ECA-ratio.”

Reconstructed catalyst layer microstructure.— In the bilayer catalyst layer, two catalyst-coated membrane (CCM) layers, **A** and **B**, of thickness around $5 \mu\text{m}$ each are physically juxtaposed to develop the catalyst layer. Catalyst layers **A** and **B** have the same Pt

loadings, but different I/C (ionomer to carbon) weight ratios of 0.417 and 0.667, respectively. By placing **A** and **B** either close to the membrane or close to the GDL, two different composite CLs with stair-step structures, in terms of nominal composition volume fractions, can be prepared. These two composite structures are hereafter referred to as **A/B CL** or **B/A CL** as illustrated in Fig. 1.

Before generating the respective microstructures, the pore volume fraction, ε_{CL} , and the electrolyte volume fraction, $\varepsilon_{\text{Nafion}}$, of each of the CLs are evaluated using the following relations

$$\varepsilon_{\text{CL}} = 1 - \left[\frac{1}{\rho_{\text{Pt}}} + \frac{R_{\text{C/Pt}}}{\rho_{\text{c}}} + \frac{R_{\text{C/Pt}}R_{\text{I/C}}}{\rho_{\text{Nafion}}} \right] \frac{L_{\text{Pt}}}{\Delta X_{\text{CL}}} \quad [4]$$

$$\varepsilon_{\text{Nafion}} = \left[\frac{R_{\text{C/Pt}}R_{\text{I/C}}}{\rho_{\text{Nafion}}} \right] \frac{L_{\text{Pt}}}{\Delta X_{\text{CL}}}$$

where ρ_{Nafion} , ρ_{Pt} , and ρ_{c} are the density of Nafion, Pt, and carbon, respectively. $R_{\text{I/C}}$ is the weight ratio of ionomer to carbon, $R_{\text{C/Pt}}$ is the weight ratio of carbon to Pt in 40% Pt/C catalyst, L_{Pt} is the Pt loading and ΔX_{CL} is the thickness of each sublayer. Now, using Eq. 4, with $\Delta X_{\text{CL}} = 5 \mu\text{m}$, $L_{\text{Pt}} = 0.199 \text{ mgPt/cm}^2$, $R_{\text{C/Pt}} = 1.5$, $\rho_{\text{Nafion}} = \rho_{\text{c}} = 2 \text{ g/cc}$ and $\rho_{\text{Pt}} = 21.5 \text{ g/cc}$, the electrolyte and pore volume fractions for CL-A and CL-B can be calculated as

$$\begin{aligned} \varepsilon_{\text{CL/A}} &= 0.56, & \varepsilon_{\text{Nafion/A}} &= 0.12 \\ \varepsilon_{\text{CL/B}} &= 0.48, & \varepsilon_{\text{Nafion/B}} &= 0.2 \end{aligned} \quad [5]$$

Now, using the volume fractions of pore, electrolyte, and electronic phases, the microstructures of **A/B CL** and **B/A CL** are reconstructed using the stochastic generation method detailed earlier. It is to be noted that for simplicity, the two-point autocorrelation function evaluated from a 2-D TEM image of a CCM CL-A is used for the CCM CL-B as well for the reconstruction of the **A/B** and **B/A CLs**. This simplification could be well justified since both the **A/B** and **B/A CLs** exhibit very similar electrochemically active interfacial area ratio (~ 29) measured using cyclic voltammetry, which, in turn, indicates that a very similar pore-space correlation would suffice for a reasonable two-phase reconstruction. Figure 2 shows the reconstructed microstructure of the **A/B CL** and the corresponding 2-D TEM image used for evaluation of the autocorrelation function. Figure 3 represents the distributions of cross-sectional averaged pore and electrolyte volume fractions across the CL thickness for the **A/B CL**. Figures 4 and 5 show the reconstructed **B/A CL** and the corresponding cross-sectional averaged pore/electrolyte volume fraction distributions across the CL thickness, respectively. Several 3-D structures are generated with varying number of unit cells. However, the reconstructed microstructure with the electrochemically active interfacial area ratio complying closely with the experimentally measured value using cyclic voltammetry is selected for the subsequent DNS calculations. The reconstructed, 3-D microstructure with 100 elements in the thickness direction and 50 elements each in the spanwise directions produces an active interfacial area ratio of around 30, which matches reasonably well with the measured value

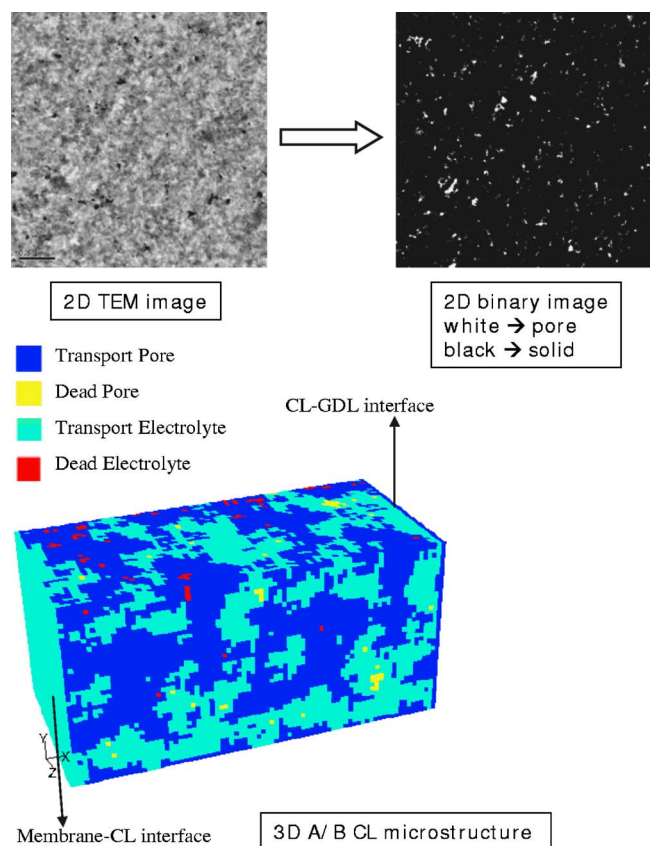


Figure 2. (Color online) Reconstructed A/B CL microstructure and the input CL TEM image.

(~29) and thereby reproduces the most important structural parameter responsible for electrochemical activity of the CL. Furthermore, in this paper, the focus is on the applicability of the DNS model in understanding the performance of a bilayer CL structure from a pore-scale perspective. The investigation of statistical influence of

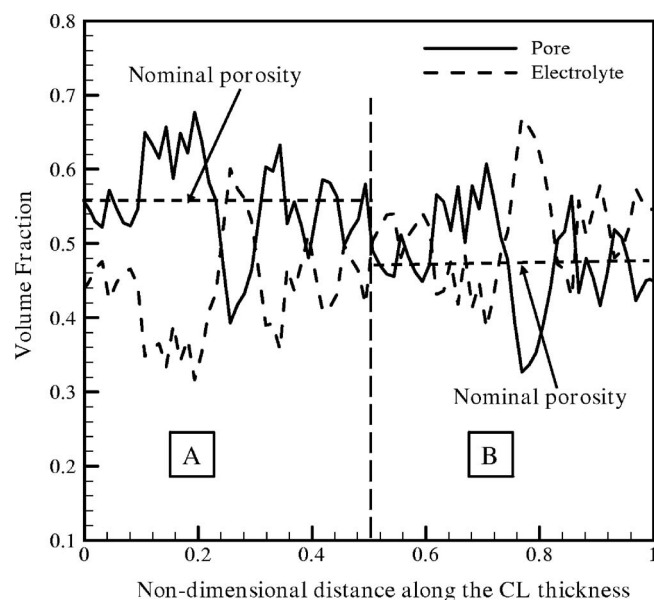


Figure 3. Cross-sectional averaged void and electrolyte phase volume fractions across the A/B CL thickness.

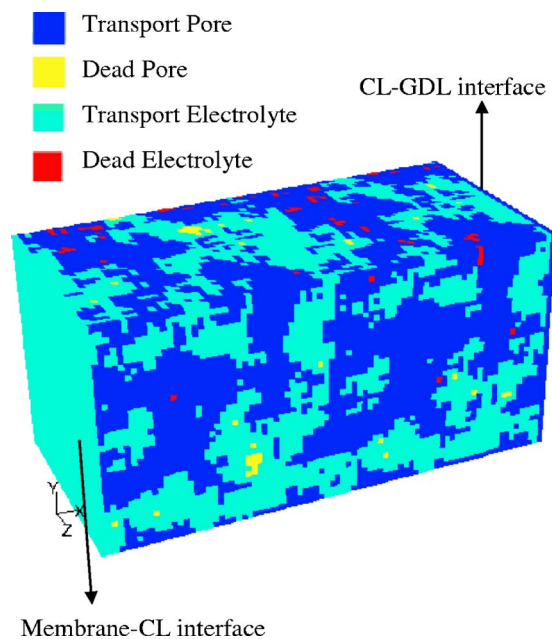


Figure 4. (Color online) Reconstructed B/A CL microstructure.

the microstructure reconstruction on the underlying transport phenomena is currently underway and is envisioned to reveal some statistics of the pore-path and proton-path tortuosity of the PEFC CL structures fabricated using the CCM (catalyst-coated membrane) and CDM (catalyzed diffusion medium) methods.

Transport processes and model assumptions.— The salient transport processes considered in the present study are (i) oxygen and water vapor diffusion through the transport pore phase, (ii) proton transport through the transport electrolyte phase, and (iii) ORR at the electrochemically active interface.

Additionally, the water transport mechanism considered in this study needs special elucidation. Water is transported from the anode through the membrane by the electro-osmotic drag, expressed by

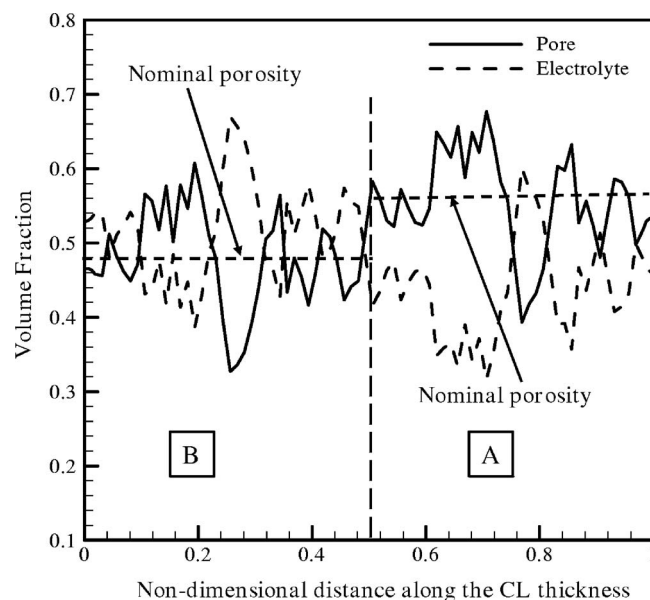


Figure 5. Cross-sectional averaged void and electrolyte phase volume fractions across the B/A CL thickness.

$$N_{w,drag} = n_d N_{H^+} = n_d \frac{I}{F} \quad [6]$$

The electro-osmotic drag coefficient, n_d , denoting the number of water molecules carried by each proton (H^+) across the membrane as current is passed, varies with the degree of membrane hydration according to the experimental measurements by Zawodzinski et al.²⁸ In the present study, a constant drag coefficient of unity is used because the water content of interest ranges from zero to 14 for a partially hydrated membrane. The water generation in the cathode CL due to ORR results in water back diffusion to the anode across the membrane owing to the concentration gradient.

The chief assumptions made in the current DNS model are (i) isothermal and steady state operation; (ii) existence of thermodynamic equilibrium at the reaction interface between the oxygen concentration in the gas phase and that dissolved in the electrolyte phase, i.e., negligible oxygen diffusion in the electrolyte phase due to the small ionomer film thickness (~ 2 nm), as approximately estimated by Kocha,²⁹ covering the C/Pt surface; (iii) water is in the gas phase even if water vapor concentration slightly exceeds the saturation value corresponding to the cell operation temperature (i.e., slight oversaturation is allowed); (iv) water in the electrolyte phase is in equilibrium with the water vapor, thus water transport through the gas phase is only considered and the electro-osmotic drag due to water through the electrolyte phase in the CL is neglected; and (v) uniform electronic phase potential since the electrode is very thin and its electronic conductivity is very high and, hence, the electron transport is not considered. The ionic conductivity of the mixed phase is thus normalized with respect to the electrolyte phase volume fraction as follows²⁴

$$\kappa = \kappa_0 \cdot \left(\frac{\epsilon_e}{\epsilon_e + \epsilon_s} \right)^{1.5} = \kappa_0 \cdot \left(\frac{\epsilon_e}{1 - \epsilon_g} \right)^{1.5} \quad [7]$$

where κ_0 is the intrinsic conductivity of the electrolyte phase, ϵ_e , ϵ_s , and ϵ_g are the electrolyte phase, electronic phase, and gas pore volume fractions, respectively. It should be noted that the aforementioned Bruggeman-like correction factor in the effective, intrinsic ionic conductivity is strictly due to the mixed electrolyte/electronic phase assumption in the two-phase reconstruction model. However, similar to the pore-path tortuosity owing to the underlying structure, the local variation of the electrolyte phase volume fraction and its impact on the proton-path tortuosity are still enforced via the reconstruction model as evidenced by the local variations of the solid phase volume fractions in Fig. 3 and 5. Advancing the current two-phase reconstruction model to a three-phase description depends on the available phase resolution of the state-of-the-art TEM characterization of the CL structures. A distinct three-phase resolution of the CL micrographs will enable the description of separate electrolyte and electronic phases in the microstructure reconstruction model and subsequently aid to the inclusion of water transport via electro-osmotic drag in the CL membrane phase within the framework of the DNS model. These advancements are envisioned as future tasks to the current DNS model.

Governing equations.—The governing differential equations valid for all the phases are developed based on the single-domain approach, which does not require the specification of internal boundary conditions at the phase interfaces. Because of slow kinetics of the ORR, the electrochemical reaction is described by the Tafel kinetics as follows

$$j = -i_0 \left(\frac{c_{O_2}}{c_{O_2,ref}} \right) \exp \left(\frac{-\alpha_c F}{RT} \eta \right) \quad [8]$$

where i_0 is the exchange current density, c_{O_2} and $c_{O_2,ref}$ refer to local oxygen concentration and reference oxygen concentration respectively, α_c is the cathode transfer coefficient for the ORR, F is the Faraday's constant, R is the universal gas constant, and T is the cell operating temperature. A value of 50 nA/cm² for the exchange cur-

rent density is used in the present calculations. The overpotential η is defined as

$$\eta = \phi_s - \phi_e - U_0 \quad [9]$$

where ϕ_s and ϕ_e refer to the electronic and electrolyte phase potentials at the reaction sites, respectively. U_0 is the reference open-circuit potential of the cathode under the cell operation temperature.

The conservation equations for the transport of proton, O_2 , and water vapor, respectively, can be expressed as follows²⁴

$$\nabla \cdot (\kappa_e \nabla \phi_e) + S_\phi = 0 \quad [10]$$

$$\nabla \cdot (D_{O_2}^g \nabla c_{O_2}) + S_{O_2} = 0 \quad [11]$$

$$\nabla \cdot (D_{H_2O}^g \nabla c_{H_2O}) + S_{H_2O} = 0 \quad [12]$$

The second term in Eq. 10-12 represents a source/sink term at the catalyzed interface where the electrochemical reaction takes place. Details about the source/sink terms as well as the single-domain formulation through a discrete phase function can be found in Ref. 24.

The transfer current between the two neighboring cells forming an active interface is described by the Tafel equation as follows²⁴

$$j = i_0 \frac{c_{O_2}(i+1,j,k)}{c_{O_2,ref}^g} \exp \left[\frac{\alpha_c F}{RT} \phi_e(i,j,k) \right] \text{ (A/cm}^2\text{)} \quad [13]$$

$\phi_e(i,j,k)$ is used to represent the cathode overpotential in the kinetic expression since both the open-circuit potential and the electronic phase potential are constant. It is worth mentioning that i_0 represents the modified exchange current density after expressing the overpotential, η , in terms of phase potential and open circuit potential as given by Eq. 9.

Boundary conditions.—In order for convenience in implementing the boundary conditions, at the membrane-CL interface (i.e., the left boundary) and at the CL-GDL interface (i.e., at the right boundary), one layer of electrolyte-only and pore-only cells are added to the computational domain, respectively. In the y and z directions, symmetry boundary conditions are applied. In summary, the boundary conditions are as follows²⁴

$$y = 0, \quad y = y_L, \quad z = 0, \quad z = z_L, \quad \frac{\partial c_{O_2}}{\partial n} = 0, \quad \frac{\partial c_{H_2O}}{\partial n} = 0, \quad \frac{\partial \phi_e}{\partial n} = 0 \quad [14]$$

$$x = 0 \text{ (i.e., membrane-CL interface),} \quad \frac{\partial c_{O_2}}{\partial n} = 0,$$

$$\frac{\partial c_{H_2O}}{\partial n} = -\frac{N_{w,net}}{D_{H_2O}}, \quad -\kappa \frac{\partial \phi_e}{\partial n} = I \quad [15]$$

$$x = x_L \text{ (i.e., CL-GDL interface),} \quad c_{O_2} = c_{O_2,0},$$

$$c_{H_2O} = c_{H_2O,0}, \quad \frac{\partial \phi_e}{\partial n} = 0 \quad [16]$$

The oxygen concentration at the CL-GDL interface is evaluated using the oxygen concentration in the gas channel and duly adjusting it with respect to the diffusion resistance through the GDL. The oxygen concentration in the gas channel is assumed constant, thus, representative of a physically large stoichiometric flow rate. The oxygen concentration at the CL-GDL interface can be expressed as²⁴

Table I. DNS model input parameters.

Parameter	Value
Oxygen diffusion coefficient in air, $D_{O_2}^g$ (m ² /s)	9.5×10^{-6}
Water vapor diffusivity in air, $D_{H_2O}^g$ (m ² /s)	1.28×10^{-5}
Pressure at the gas channel inlet, \bar{p} (kPa)	200
GDL thickness, ΔX_{GDL} (μ m)	290
GDL porosity, ε_{GDL}	0.6
GDL tortuosity, τ_{GDL}	1.5

$$c_{O_2,0} = c_{O_2,inlet} - \frac{I\Delta X_{GDL}}{4FD_{O_2,GDL}^{g,eff}} \quad [17]$$

The oxygen concentration profile through the GDL is assumed linear and $D_{O_2,GDL}^{g,eff}$ is the effective diffusion coefficient of oxygen adjusted with respect to the GDL porosity ε_{GDL} and tortuosity τ_{GDL} and is given by²⁴

$$D_{O_2,GDL}^{g,eff} = D_{O_2}^g \frac{\varepsilon_{GDL}}{\tau_{GDL}} \quad [18]$$

At the membrane–CL interface, a net water transport coefficient α is employed that takes into account the net water flux across the membrane due to the electro-osmotic drag and back diffusion effects, and can be expressed as²⁴

$$N_{w,net} = \alpha \frac{I}{F} = N_{w,drag} - N_{w,dif} \quad [19]$$

where $N_{w,dif}$ is the water flux through the membrane due to back diffusion from the cathode side to the anode side. In the present study, α is assumed to be constant although it depends on a number of parameters, including the cell temperature and humidity conditions at anode and cathode inlets, to name a few. The assumed value of $\alpha = 0.2$ is simply a boundary condition input parameter for the CL-only model. The influence of different α values on the CL transport has been demonstrated in our recent DNS model paper in Ref. 30. Thus the boundary condition at the membrane–CL interface is given by²⁴

$$\left. \frac{\partial c_{H_2O}}{\partial x} \right|_{x=0} = \frac{-N_{w,net}}{D_{H_2O}^g} \quad [20]$$

Similar to the treatment of the oxygen concentration boundary condition, the water vapor concentration CL–GDL interface is calculated from the concentration of water vapor at the channel inlet with correction for diffusion resistance in the GDL and is given by²⁴

$$c_{H_2O}|_{x=x_L} = c_{H_2O,inlet} + N_w|_{x=x_L} \frac{\Delta X_{GDL}}{D_{H_2O,GDL}^{g,eff}} \quad [21]$$

The effective diffusion coefficient of water vapor in the gas phase through the GDL is evaluated similar to the oxygen diffusion coefficient given by Eq. 18. The water flux through the GDL is the sum of the net flux across the membrane and the water production rate in the catalyst layer and can be expressed as²⁴

$$N_w|_{x=x_L} = N_{w,net} + N_{w,prod} = (\alpha + 0.5) \frac{I}{F} \quad [22]$$

From the inlet relative humidity (RH), water vapor concentration of the humidified air at the channel inlet is calculated by²⁴

$$c_{H_2O,inlet} = RH c_{H_2O}^{sat} \quad [23]$$

where $c_{H_2O}^{sat}$ is the saturation concentration of water at the cell operating temperature.

Model input parameters.— The operating, geometric and transport parameters used in the present study are summarized in Table I.

However, two transport parameters, namely, the proton conductivity and species diffusivity are explained below for clarity.

Proton conductivity.— The proton conductivity of the electrolyte phase, i.e., Nafion, as a function of water content, has been correlated by Springer et al.³¹ from experiments as

$$\kappa_0(\lambda) = 100 \exp \left[1268 \left(\frac{1}{303} - \frac{1}{T} \right) \right] (0.005139\lambda - 0.00326) \text{ (S/m)} \quad [24]$$

where the water content in the membrane λ depends on the water activity a in the gas phase according to the following experimental data fit

$$\lambda = \begin{cases} 0.043 + 17.81a - 39.85a^2 + 36.0a^3 & \text{for } 0 < a \leq 1 \\ 14 + 1.4(a - 1) & \text{for } 1 < a \leq 3 \end{cases} \quad [25]$$

The water activity a is defined as

$$a = \frac{c_{H_2O}}{c_{H_2O}^{sat}} \quad [26]$$

Substitution of Eq. 25 into Eq. 24 provides the variation of proton conductivity in Nafion with water activity. Thus, the proton conductivity varies at every point within the CL with the variation of water vapor concentration.

Species diffusivity.— The binary diffusion coefficient of species (i.e., oxygen and water vapor) i in the gas phase depends on temperature and pressure and is given by³²

$$D_{b,i}^g = D_{b,i,0}^g \left(\frac{T}{T_0} \right)^{3/2} \left(\frac{p_0}{p} \right) \quad [27]$$

In the present study, the reference pressure p_0 is taken as 1 atm and the reference temperature T_0 as 273 K. However, for the pore-level DNS modeling in the catalyst layer microstructure, Knudsen diffusion due to molecule-to-wall collision, as opposed to molecule-to-molecule collision in bulk diffusion, becomes important. Therefore, in the present model, a combined diffusivity of species i in the gas phase is employed and can be expressed as²¹

$$D_i^g = \left(\frac{1}{D_{b,i}^g} + \frac{1}{D_{K,i}} \right)^{-1} \quad [28]$$

$D_{K,i}$ is the Knudsen diffusion coefficient, which is of the same order of magnitude as the binary diffusion coefficient for the CL, and can be computed according to the kinetic theory of gases as²¹

$$D_{K,i} = \frac{2}{3} \left(\frac{8RT}{\pi M_i} \right)^{1/2} r_p \quad [29]$$

where a representative mean pore radius, r_p , of 50 nm is used in the current model. The assumption of the representative pore radius is intended to reduce the computational complexity of the DNS model. The pore size distribution and, hence, the local pore radii can be evaluated from the reconstructed 3-D microstructure using the concept of granulometry, which has been demonstrated in our recent work on transport through reconstructed fibrous diffusion media in Ref. 33, and subsequently can be incorporated into Eq. 29. However, the impact of the pore size distribution on Knudsen diffusion in a reconstructed CL structure using the DNS model is left as a future exercise.

Solution methodology.— The conservation equations, Eq. 10-12, are discretized using a finite volume approach³⁴ and solved using the commercial CFD software Fluent.³⁵ The user-defined function (UDF) capability in Fluent³⁵ is deployed to customize the source terms and to solve the set of governing equations within the framework of scalar transport equations. In the present study, for the (10 μ m \times 5 μ m \times 5 μ m) CL structure, the number of cells within the computational domain in the x , y , and z directions are 100

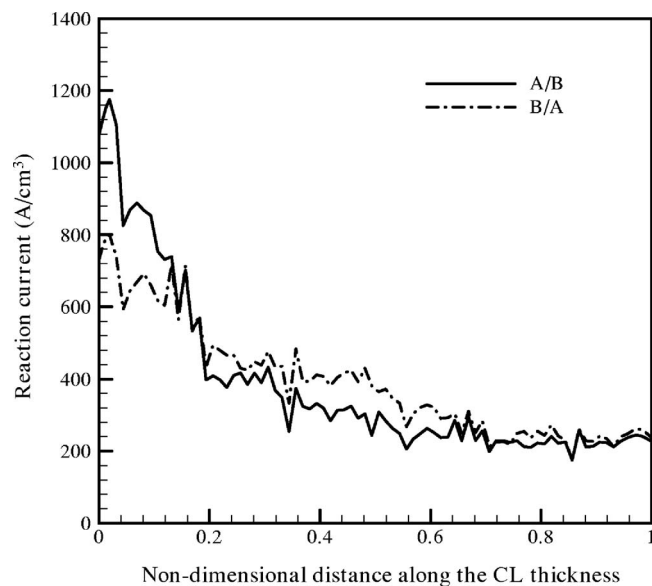


Figure 6. Cross-sectional averaged reaction current distribution along the CL thickness at 70°C, 100% inlet RH, and 0.4 A/cm².

× 50 × 50, respectively. Convergence was considered achieved when the relative error between two consecutive iterations reached 10⁻⁶ for each scalar field. A typical simulation for a particular current density, on a DELL PC with Pentium 4 processor, 1 GB RAM, 2.79 GHz processor speed, takes ~6 h to converge.

Results and Discussion

Baseline simulation predictions.— Figures 6 and 7 show the cross-sectional averaged reaction current and cathode overpotential distributions along the CL thickness, respectively, for the A/B and B/A CLs with 100% relative humidity (RH) air, at 70°C cell operation temperature, 200 kPa inlet pressure, and current density of 0.4 A/cm². The catalyst layer performance is influenced by two competing factors, namely, protonic resistance and oxygen transport. Higher ionomer volume fraction reduces protonic resistance while

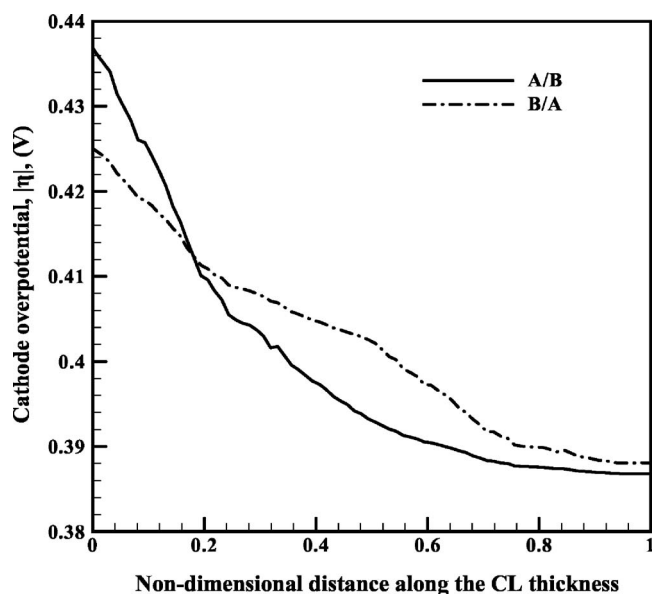


Figure 7. Cross-sectional averaged overpotential distribution along the CL thickness at 70°C, 100% inlet RH, and 0.4 A/cm².

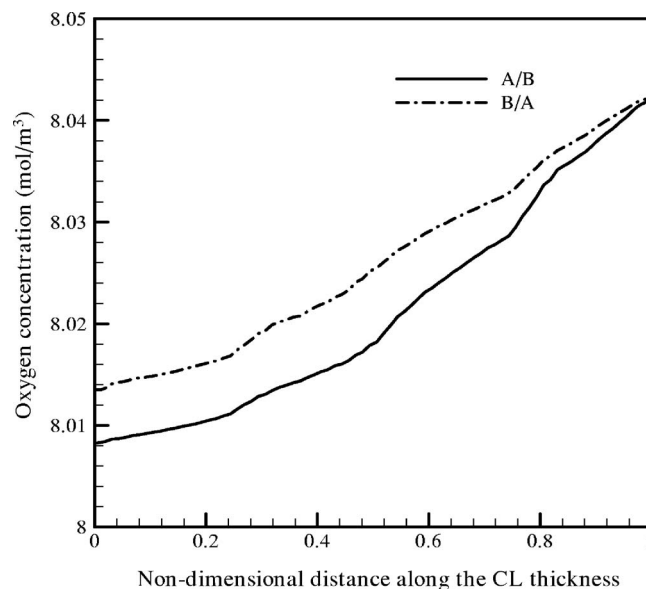


Figure 8. Cross-sectional averaged oxygen concentration distribution along the CL thickness at 70°C, 100% inlet RH, and 0.4 A/cm².

higher pore volume fraction favors oxygen transport. In the B/A CL, near the membrane–CL interface, higher ionomer content reduces protonic resistance, which, in turn, aids in the reduction of cathode overpotential and results in an extended reaction zone as is evident from the reaction current distribution. In the A/B CL, due to increased protonic resistance resulting from lower ionomer content in the vicinity of the membrane–CL interface and in order to overcome the corresponding higher overpotential, the reaction zone is concentrated to a relatively smaller region as compared to the B/A CL. Although the benefit of higher ionomer volume fraction near the membrane–CL interface is clearly pronounced via reduced overpotential and extended reaction zone from Fig. 6 and 7 at low current density (i.e., 0.4 A/cm²), where transport limitation is primarily due to hindered proton transport, the resulting reaction current distribution due to the varying ionomer content could also be harnessed to enhance cell performance at higher current density, where transport limitation owing to hindered oxygen transport will dominate. For the B/A CL, even at higher current density, there might still be some active reaction sites due to an extended reaction zone, resulting from a favorable distribution of the ionomer content along the CL thickness, and thus will exhibit a higher limiting current density as compared to the A/B CL. Furthermore, a higher pore volume fraction near the CL–GDL interface in the B/A CL will aid in enhanced oxygen transport. In the A/B CL, the concentration of the active reaction zone toward the vicinity of the membrane–CL interface as well as relatively lower void phase fraction near the CL–GDL interface will negatively impact the transport of oxygen to the reaction sites at higher current density and subsequently will exhibit a lower limiting current and, hence, a poorer performance as compared to the B/A CL. Figures 8 and 9 show the cross-sectional averaged oxygen and water vapor concentration along the CL thickness, respectively, for both the A/B and B/A CLs. The oxygen concentration profile for the A/B CL exhibits higher depletion in the vicinity of the membrane–CL interface as compared to the B/A CL, whereas the water concentration profile shows the opposite trend. The negligible difference in the oxygen concentration values at the membrane–CL interface between the two CLs further highlight the proton transport limiting regime characterized by 0.4 A/cm². These observations corroborate with the corresponding reaction current distribution profiles as explained earlier.

The simulated polarization curves with air as the oxidant under the aforementioned operating conditions are shown in Fig. 10, along

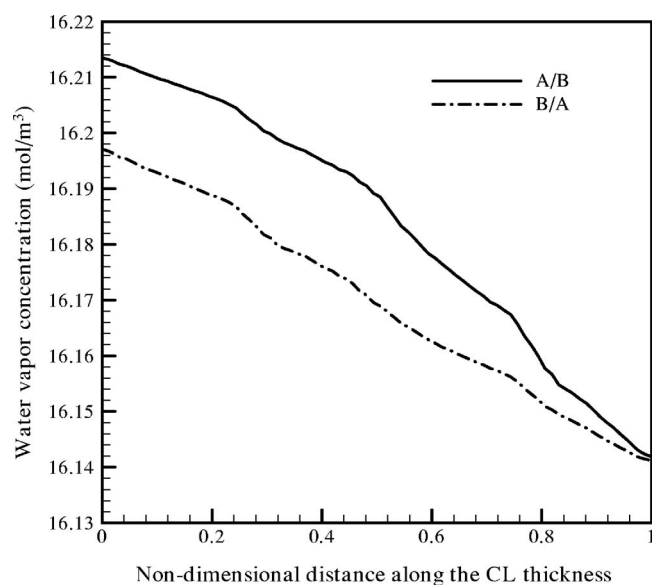


Figure 9. Cross-sectional averaged water vapor concentration distribution along the CL thickness at 70°C, 100% inlet RH, and 0.4 A/cm².

with the corresponding experimental data. The “polarization curve” refers to the cathode overpotential vs current density curve in the present study and hence is different from the standard I - V curve otherwise used popularly in the literature. As a general trend, the predicted cathode polarization curves by the DNS model depict a fast drop in the small current density region controlled by the ORR kinetics followed by a linear voltage drop in the mixed control regime and, finally, at higher current densities (~ 1 A/cm²), the mass transport limitation appears with a fast voltage drop resulting from oxygen depletion. The experimental polarization curves were obtained from electrochemical performance evaluations conducted in a 5 cm² graphite cell fixture with identical anode and cathode single-pass, serpentine flow fields with computer-controllable test parameters, such as temperature, pressure, fuel/oxidant flow rates, current and cell voltage, using a fuel cell test stand (Arbin, TX), and is detailed in Ref. 36. The cell was operated at 70°C, 200 kPa, and

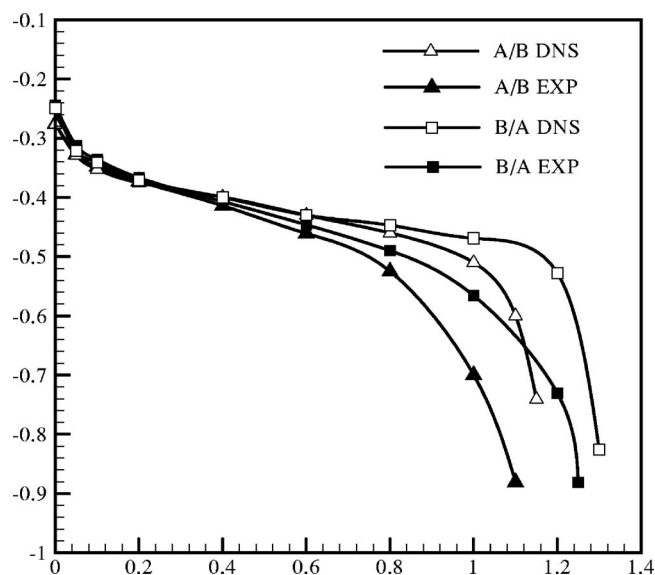


Figure 10. Polarization curves for A/B and B/A CLs. Operating conditions: 70°C, 200 kPa, and 100% RH.

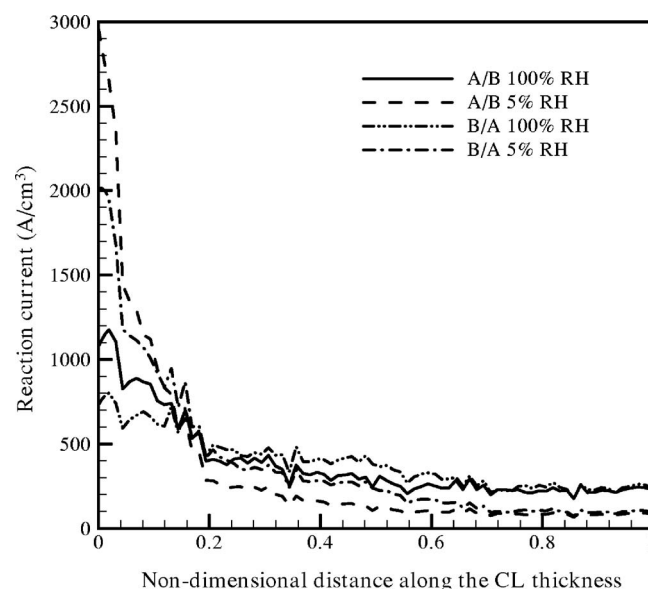


Figure 11. Cross-sectional averaged reaction current distribution along the CL thickness for different inlet humidity at 70°C and 0.4 A/cm².

100% RH conditions at both anode and cathode sides with fixed flow rates of hydrogen and air. The experimentally obtained cell voltage (V_{cell}) vs current density I data was further processed to extract the variation of cathode overpotential η_c with current density according to the following relation

$$\eta_c = V_{\text{cell}} + I \times \text{HFR} - U_0 \quad [30]$$

where HFR refers to the high-frequency resistance measured experimentally and U_0 is the thermodynamic equilibrium potential corresponding to the fuel cell operating temperature. It is important to note that in the above equation, the anodic overpotential for hydrogen oxidation and protonic resistance in the anode catalyst layer are assumed to be negligible. The local cathode overpotential is obtained directly from the solution of Eq. 10, as explained in the Governing Equations section and also detailed in our earlier DNS model paper,²⁴ and is volume averaged over the computational domain for the predicted polarization curve in Fig. 10. It is clear from Fig. 10 that there are reasonable agreements between the DNS predictions and experimental observations in the kinetic-control and ohmic-control regimes. However, both for A/B and B/A CLs, the ohmic-control regime seems to be slightly extended in the DNS calculations. Because water transport has been modeled only in the gas phase and the effect of liquid water transport in the CL is not considered, the DNS model overpredicts the ohmic-control regime. Finally, from Fig. 10, it is evident that the DNS calculations show better performance for the B/A CL as compared to the A/B CL in accordance with the experimental observations and conforms to the explanations provided earlier with respect to the relative distributions of ionomer and pore volume fractions in the CL and the resulting reaction current distributions. Finally, it can be inferred that a higher ionomer content near the membrane-CL interface along with a higher void fraction near the CL-GDL interface prove to be beneficial for a bilayer CL performance.

Effect of inlet air humidity.— Figures 11 and 12 show the cross-sectional averaged reaction current and cathode overpotential distributions across the CL thickness, respectively, with air as the oxidant at 5% and 100% RH, at 70°C cell operation temperature, 200 kPa inlet pressure, and current density of 0.4 A/cm². From the cathode overpotential distributions, it is evident that low humidity operation results in enhanced voltage drop. This is primarily due to the poorer proton conductivity associated with the partially hydrated electrolyte phase, leading to enhanced protonic resistance. At 100% RH, the

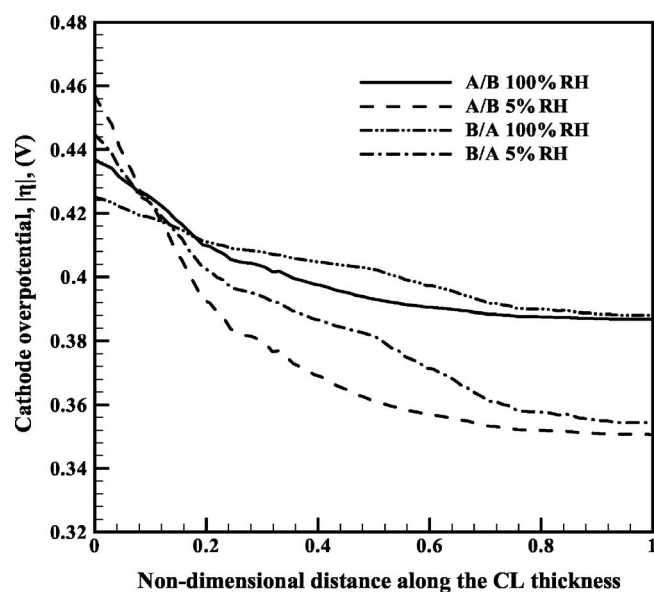


Figure 12. Cross-sectional averaged overpotential distribution along the CL thickness for different inlet humidity at 70°C and 0.4 A/cm².

electrolyte phase remains fully humidified with saturated water vapor while the water vapor concentration is significantly reduced at 5% RH, causing increased ohmic resistance. The enhanced protonic resistance at low humidity further exacerbates the performance of the A/B CL, where the reaction zone further shifts toward the vicinity of the membrane–CL interface as compared to that for the 100% RH operation. In the A/B CL, at 5% RH operation, the lower electrolyte phase volume fraction near the membrane–CL interface along with the reduced ionic conductivity owing to low humidity result in significantly higher protonic resistance, which, in turn, increases the overpotential. In order to overcome the localized elevated overpotential, the reaction zone shrinks further and concentrates primarily in the 10–15% of the CL thickness near the membrane–CL interface in the A/B CL. Overall, it can be conjectured that low humidity operation leads to a steeper overpotential gradient as well as an apparent reduction in the active reaction zone extent as compared to that in the fully humidified operation. Figures 13 and 14 exhibit the 3-D reaction current contours at different inlet relative humidity for the A/B CL and B/A CL, respectively. It can be observed that low humidity operation indeed causes reaction current snap off and renders a significant portion of the CL virtually inactive, which is however more pronounced for the A/B CL as explained earlier. At fully humidified operation, the reaction current contours show that high value of reaction current (represented by the red color map in the contours) prevails over significant portion of the B/A CL as compared to the A/B CL and further emphasizes the importance of the current DNS model in elucidating detailed pore-scale description of underlying transport through the CL microstructures. It should be noted that in order to highlight the extent of the active reaction zone and to compare among different RH operations, a lower threshold value of the reaction current, e.g., 350 A/cm³ for the 5% RH operation and 650 A/cm³ for the 100% RH operation, is set and is evidenced by the corresponding color maps in the 3-D reaction current distributions in Fig. 13 and 14. Furthermore, it is worth mentioning that although low-humidity operation might extend the ohmic control regime slightly thereby delaying the onset of the transport limitation characterized by higher current density operation, the unfavorable void fraction distribution near the CL–GDL interface as well as the shift of the active reaction zone toward the membrane–CL interface in the A/B CL will inhibit oxygen transport and would finally exhibit poorer performance as compared to the B/A CL, similar to that in the 100% RH operation. Because the

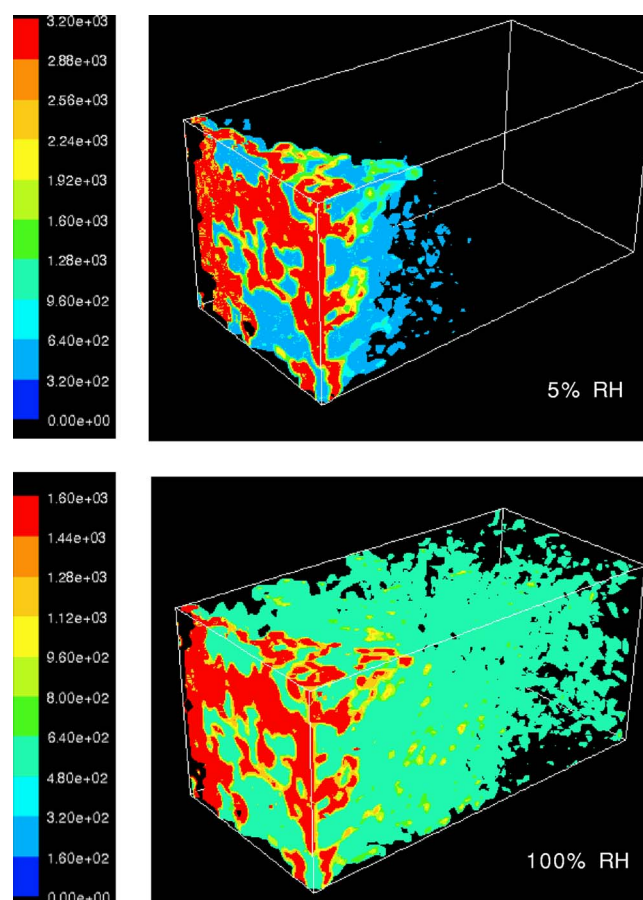


Figure 13. (Color online) 3-D reaction current distribution contours for different inlet humidity at 70°C and 0.4 A/cm² for the A/B CL.

focus of this article is to provide a pore-scale description of the influence of the ionomer and void fraction variations on the local reaction current distributions in the CL, therefore, the global performance curves, e.g., the polarization curves for different RH values, are skipped here, which is however detailed in our recent DNS work³⁰ for the single-layer CL.

Effect of cell operating temperature.— In order to investigate the effect of elevated cell temperature on the bilayer CL performance, DNS calculations are performed for the A/B and B/A CLs with air as the oxidant, at 95°C operating temperature, 200 kPa inlet pressure, and 50% inlet RH. It is worth mentioning that the correlation between the proton conductivity of the electrolyte phase and water content in Eq. 24 is assumed valid at high-temperature operation as well.³⁷ Additionally, temperature dependence of the relevant physicoelectrochemical properties (e.g., species diffusivity, exchange current density, etc.) is appropriately considered in the present study.

Figures 15 and 16 show the cross-sectional averaged reaction current and overpotential distributions at different cell operating temperatures across the CL thickness, respectively, for the A/B and B/A CLs at 0.4 A/cm² and 50% inlet RH. From the overpotential distribution, it is evident that at elevated operating temperature, both the CLs exhibit higher voltage loss as compared to that at lower cell temperature. At 95°C, the saturation concentration of water vapor is around three times that at 70°C. The higher value of saturation concentration at 95°C leads to lower water activity, given by Eq. 26, which, in turn, results in significantly lower ionic conductivity of the electrolyte phase, demonstrated by Eq. 24 and 25, as compared to that at 70°C. Therefore, at the representative current density under investigation, both the CLs show poorer performance at elevated

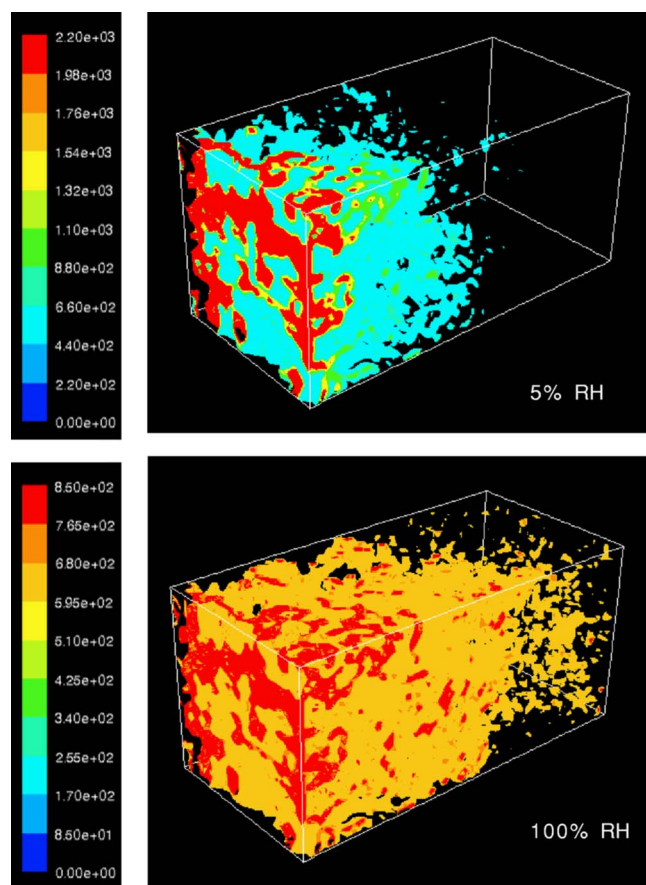


Figure 14. (Color online) 3-D reaction current distribution contours for different inlet humidity at 70°C and 0.4 A/cm² for the B/A CL.

temperature operation. The situation is further aggravated for the A/B CL with unfavorable electrolyte phase volume fraction gradient as explained earlier and manifests in terms of a surge in reaction

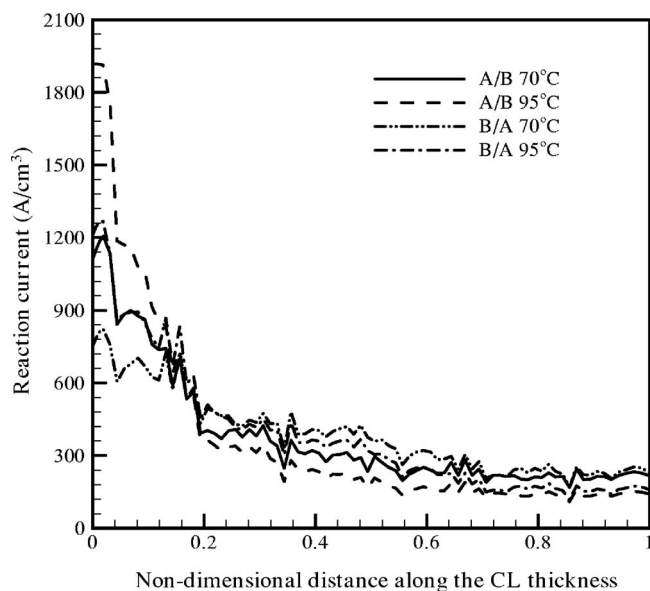


Figure 15. Cross-sectional averaged reaction current distribution along the CL thickness for different cell operating temperatures at 50% inlet RH and 0.4 A/cm².

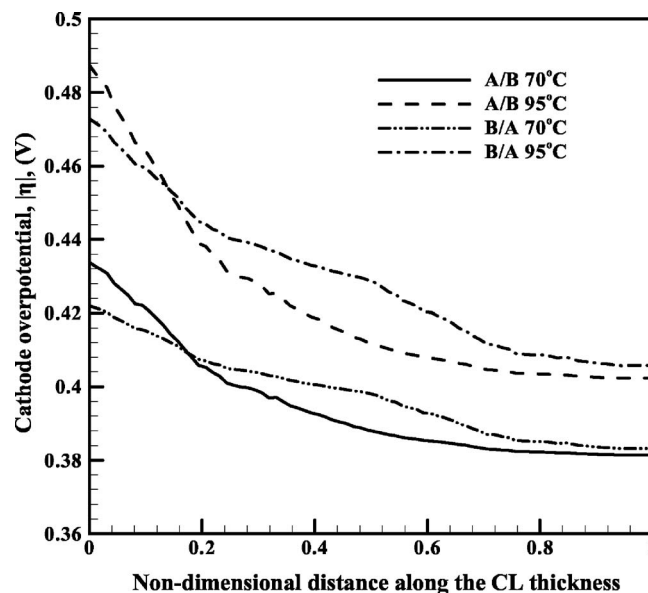


Figure 16. Cross-sectional averaged overpotential distribution along the CL thickness for different cell operating temperatures at 50% inlet RH and 0.4 A/cm².

current in the immediate neighborhood of the membrane–CL interface in order to overcome the localized elevated overpotential barrier, which translates into a significant reduction in the reaction zone extent. This observation can be further illustrated with the corresponding 3-D contours of the reaction current distributions as shown in Fig. 17 and 18 for the A/B and B/A CLs, respectively. Similar to the different RH calculations, a lower threshold value of the reaction current, e.g., 600 A/cm³ for both the temperatures and for both the CLs, is set in order to highlight the extent of the active reaction zone and for comparison across different temperature operations, which is evidenced by the corresponding contour colormaps in Fig. 17 and 18. Furthermore, in the case of elevated temperature operation, it is important to note that higher saturation concentration of water vapor results in lower oxygen concentration available for reaction due to corresponding lower partial pressure. Therefore, at higher current density operation, where transport limitation dominates, the unfavorable void fraction gradient in the A/B CL will further aid in the oxygen dilution effect due to elevated temperature and would lead to overall lower performance. Finally, apropos of the focus of the pore-scale investigations presented in this article, the polarization curves for different temperatures are skipped, which can however be found elsewhere in the literature, e.g., for single layer CL in a full cell experiment in Ref. 38. The predictions from our DNS calculations however indicate similar overall trend of the cell of performance at elevated temperature operation as reported in Ref. 38.

Conclusion

The importance of bilayer cathode catalyst layers on the PEFC performance is presented via a pore-level description of the concentration and potential fields using a DNS model. The bilayer CL structures with varied electrolyte and void phase fractions are generated using a stochastic reconstruction technique. The DNS predictions suggest that a higher electrolyte content near the membrane–CL interface exhibits enhanced performance through an extended active reaction zone and overall conforms to the experimental results. A higher pore volume fraction near the GDL improves oxygen diffusion. Additionally, the influence of the cell operating conditions in terms of the inlet RH and the cell operating temperature on the bilayer cathode CL performance is studied. Both low humidity and elevated temperature operations adversely affect the protonic conductivity and show overall lower performance as

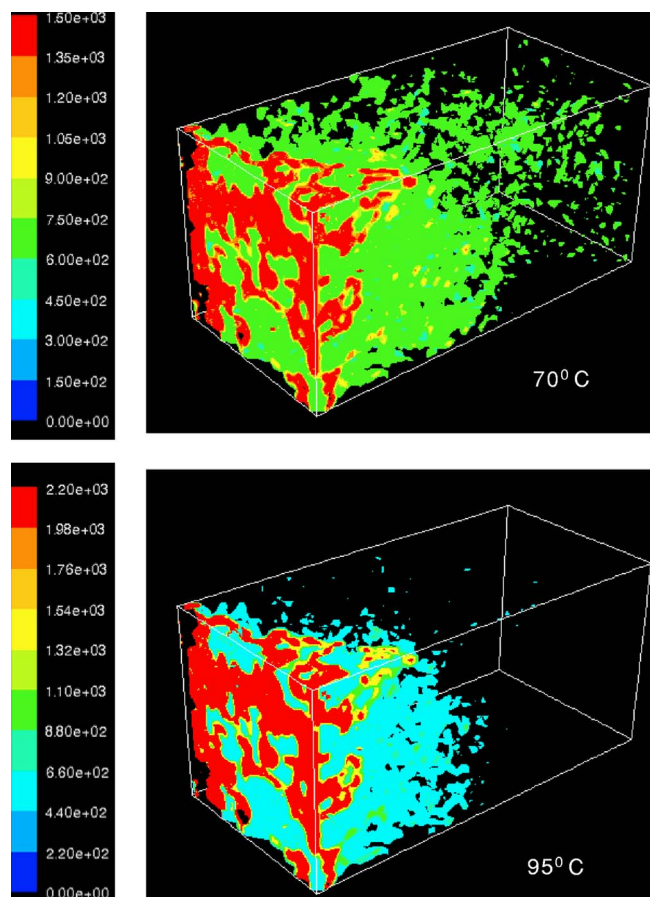


Figure 17. (Color online) 3-D reaction current distribution contours for different cell operating temperatures at 50% inlet RH and 0.4 A/cm^2 for the A/B CL.

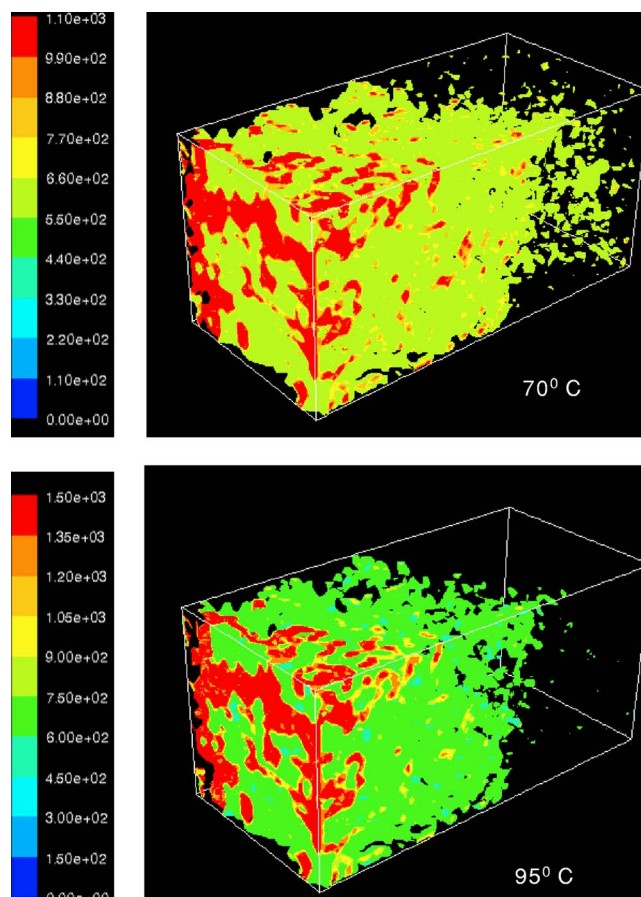


Figure 18. (Color online) 3-D reaction current distribution contours for different cell operating temperatures at 50% inlet RH and 0.4 A/cm^2 for the B/A CL.

compared to that at higher RH and lower cell temperature operations, respectively. However, the aforementioned relative distributions of the electrolyte and void phase volume fractions, namely, higher ionomer content near the membrane and higher void fraction near the GDL, still hold for better performance even in the low humidity and elevated temperature operations as well. Finally, this article attempts to provide a fresh perspective of the interdependence between the active reaction zone extent and the composition in a bilayer CL with microscopic details of the reaction current distributions within the CL structure.

Acknowledgment

The authors thank Dr. Fuqiang Liu for providing the experimental data used in Fig. 10.

The Pennsylvania State University assisted in meeting the publication costs of this article.

List of Symbols

a	water activity or specific interfacial area, cm^2/cm^3
c_i	local concentration of species i , mol/m^3
D_i	diffusion coefficient of species i , m^2/s
f	phase function for the single domain approach
F	Faraday's constant, $96,487 \text{ C/mol}$
I	current density, A/cm^2
j	reaction current density, A/cm^2
n_d	electro-osmotic drag coefficient
N_i	molar flux of species i , $\text{mol}/\text{m}^2 \text{ s}$
p	pressure, Pa
R	universal gas constant, $8,314 \text{ J/mol K}$
RH	relative humidity

S	source term in the governing equations
T	absolute temperature, K
x	x coordinate, μm
y	y coordinate, μm
z	z coordinate, μm

Greek

α	net water transport coefficient
α_c	cathodic transfer coefficient
ε_k	volume fraction of phase k in the catalyst layer
κ	electrolyte conductivity, S/m
λ	membrane water content, $\text{mol H}_2\text{O}/\text{mol SO}_3^-$
ϕ_k	electrical potential in phase k , V

Subscripts and superscripts

e	electrolyte phase
eff	effective
g	gas phase
GDL	gas diffusion layer
inlet	gas channel inlet
L	catalyst layer thickness
net	net value
O_2	oxygen
prod	water production in the cathode catalyst layer
ref	reference value
sat	saturation of water
w	water
0	boundary value at the CL-GDL interface or initial/intrinsic value

References

1. S. Gottesfeld and T. A. Zawodzinski, in *Advances in Electrochemical Science and Engineering*, C. Tobias, Editor, Vol. 5, Wiley, New York (1997).
2. M. Eikerling, A. A. Kornyshev, and A. A. Kulikovskiy, *Fuel Cell Rev.*, **2004/2005**, 15 (Dec/Jan).

3. W. K. Paik, T. E. Springer, and S. Srinivasan, *J. Electrochem. Soc.*, **136**, 644 (1989).
4. E. A. Ticianelli, T. B. G. Beery, and S. Srinivasan, *J. Appl. Electrochem.*, **21**, 597 (1991).
5. S. Mukerjee, S. Srinivasan, and A. J. Appleby, *Electrochim. Acta*, **38**, 1661 (1993).
6. M. Uchida, Y. Fukuoka, Y. Sugawara, N. Eda, and A. Ohta, *J. Electrochem. Soc.*, **143**, 2245 (1996).
7. M. Uchida, Y. Fukuoka, Y. Sugawara, H. Obara, and A. Ohta, *J. Electrochem. Soc.*, **145**, 3708 (1998).
8. E. Passalacqua, F. Lufrano, G. Squadrito, A. Patti, and L. Giorgi, *Electrochim. Acta*, **43**, 3665 (1998).
9. Z. Qi and A. Kaufman, *J. Power Sources*, **113**, 37 (2003).
10. E. Antolini, L. Giorgi, A. Pozio, and E. Passalacqua, *J. Power Sources*, **77**, 136 (1999).
11. G. Sasikumar, J. W. Ihm, and H. Ryu, *J. Power Sources*, **132**, 11 (2004).
12. C. Marr and X. Li, *J. Power Sources*, **77**, 17 (1999).
13. C. C. Boyer, R. G. Anthony, and A. J. Appleby, *J. Appl. Electrochem.*, **30**, 777 (2000).
14. M. Eikerling and A. A. Kornyshev, *J. Electroanal. Chem.*, **453**, 89 (1998).
15. M. Eikerling and A. A. Kornyshev, *J. Electroanal. Chem.*, **475**, 107 (1999).
16. D. Song, Q. Wang, Z. Liu, T. Navessin, M. Eikerling, and S. Holdcroft, *J. Power Sources*, **126**, 104 (2004).
17. O. Antoine, Y. Bultel, P. Ozil, and R. Durand, *Electrochim. Acta*, **45**, 4493 (2000).
18. D. Song, Q. Wang, Z. Liu, T. Navessin, and S. Holdcroft, *Electrochim. Acta*, **50**, 731 (2004).
19. Q. P. Wang, M. Eikerling, D. T. Song, Z. S. Liu, T. Navessin, Z. Xie, and S. Holdcroft, *J. Electrochem. Soc.*, **151**, A950 (2004).
20. Z. Xie, T. Navessin, K. Shi, R. Chow, Q. Wang, D. Song, B. Andreaus, M. Eikerling, Z. Liu, and S. Holdcroft, *J. Electrochem. Soc.*, **152**, A1171 (2005).
21. C. Y. Wang, *Chem. Rev.*, **104**, 4727 (2004).
22. G. Wang, P. P. Mukherjee, and C. Y. Wang, *Electrochim. Acta*, **51**, 3139 (2006).
23. G. Wang, P. P. Mukherjee, and C. Y. Wang, *Electrochim. Acta*, **51**, 3151 (2006).
24. P. P. Mukherjee and C. Y. Wang, *J. Electrochem. Soc.*, **153**, A840 (2006).
25. P. P. Mukherjee, G. Wang, and C. Y. Wang, in *Modern Aspects of Electrochemistry*, R. White, Editor, Vol. 40, Springer, New York (2007).
26. P. M. Adler, *Porous Media: Geometry and Transports*, Butterworth-Heinemann, Stoneham, MA (1992).
27. J. G. Berryman, *J. Appl. Phys.*, **57**, 2374 (1985).
28. T. A. Zawodzinski, J. Davey, J. Valerio, and S. Gottesfeld, *Electrochim. Acta*, **40**, 297 (1995).
29. S. S. Kocha, in *Handbook of Fuel Cells: Fundamentals, Technology and Applications*, W. Vielstich, A. Lamm, and H. A. Gasteiger, Editor, Chap. 43, Vol. 3, Wiley, New York (2003).
30. G. Wang, P. P. Mukherjee, and C. Y. Wang, *Electrochim. Acta*, **52**, 6367 (2007).
31. T. E. Springer, T. A. Zawodzinski, and S. Gottesfeld, *J. Electrochem. Soc.*, **138**, 2334 (1991).
32. R. B. Bird, W. E. Stewart, and E. N. Lightfoot, *Transport Phenomena*, 2nd ed., Wiley, New York (2002).
33. V. P. Schulz, J. Becker, A. Wiegmann, P. P. Mukherjee, and C. Y. Wang, *J. Electrochem. Soc.*, **154**, B419 (2007).
34. S. V. Patankar, *Numerical Heat Transfer and Fluid Flow*, Hemisphere, Washington, DC (1980).
35. Fluent 6 UDF Manual, Ansys-Fluent, Lebanon, NH (2006).
36. F. Liu, Private communications and ECEC internal report (2005).
37. P. K. Sinha, C. Y. Wang, and U. Beuscher, *J. Electrochem. Soc.*, **154**, B106 (2007).
38. M. M. Saleh, T. Okajima, M. Hayase, F. Kitamura, and T. Ohsaka, *J. Power Sources*, **164**, 503 (2007).